Computational Insights into Electronic Excitations, Spin-Orbit Coupling Effects, and Spin Decoherence in Cr(IV)-based Molecular Qubits

Karolina Janicka, Aleksander L. Wysocki, and Kyungwha Park*

Department of Physics, Virginia Tech, Blacksburg, Virginia, 24061 USA

E-mail: kyungwha@vt.edu

Abstract

The great success of point defects and dopants in semiconductors for quantum information processing has invigorated a search for molecules with analogous properties. Flexibility and tunability of desired properties in a large chemical space have great advantages over solid-state systems. The properties analogous to point defects were demonstrated in Cr(IV)-based molecular family, $Cr(IV)(aryl)_4$, where the electronic spin states were optically initialized, read out, and controlled. Despite this kick-start, there is still a large room for enhancing properties crucial for molecular qubits. Here we provide computational insights into key properties of the Cr(IV)-based molecules aimed at assisting chemical design of efficient molecular qubits. Using the multireference *ab-initio* methods, we investigate the electronic states of $Cr(IV)(aryl)_4$ molecules with slightly different ligands, showing that the zero-phonon line energies agree with the experiment, and that the excited spin-triplet and spin-singlet states are highly sensitive to small chemical perturbations. By adding spin-orbit interaction, we find that the

sign of the uniaxial zero-field splitting (ZFS) parameter is negative for all considered molecules, and discuss optically-induced spin initialization via non-radiative intersystem crossing. To understand electron spin decoherence, we quantify hyperfine coupling to the ^{53}Cr nuclear spin and to the ^{13}C and ^{1}H nuclear spins. We show that the splitting or broadening of the electronic spin sub-levels induced by these hyperfine interactions decreases by an order of magnitude when the molecules have a substantial transverse ZFS parameter. This feature is applicable to other integer-spin molecules in order to significantly reduce spin decoherence.

Point defect centers and dopants in wide-bandgap semiconductors have been shown to be viable options for quantum information processing.[1–10] Two representative examples are negatively charged nitrogen-vacancy (NV^-) centers in diamond,[4,11–13] and phosphorus dopants in silicon.[8–10,14] Electronic spin states of the NV^- centers can be optically initialized, read-out, and coherently controlled with long spin coherence time.[1–7] Nuclear spin states of phosphorus (^{31}P) dopants can be controlled by a gate voltage or electric field.[14] Both systems have been experimentally shown to perform quantum gate operations with high fidelity.[1–3,6–10]

Inspired by this great success, organic radicals and transition-metal-based (TM) and lanthanide-based (Ln) magnetic molecules have been tailored to have desirable properties for quantum information science applications by utilizing the versatility of chemical environment.[15–24] Either molecular electronic spin states or electronic-nuclear spin states can be considered as quantum bits (qubits) or quantum d-levels (qudits) which may be initialized, read-out, or controlled by an external magnetic field and/or electric field, or optical means. For organic donor-acceptor-radical molecules, the electronic spin states were shown to be entangled and teleported with high fidelity by using microwave pulses and photoexcitation.[15] As long as TM-based or Ln-based magnetic molecules are concerned, the hyperfine interaction between the molecular electronic spin and the TM (or Ln) nuclear spin has been mostly utilized for realization of qubits.[16–21] For vanadium(IV)-based magnetic molecules, the molecular electronic-nuclear spin states were shown to have long spin co-

herence time.[16,17] For terbium(III)-based molecules, the electronic-nuclear spin states were shown to be initialized and read-out by an external magnetic field and to be manipulated by a gate voltage within a single-molecule transistor set-up,[18] where Grover's algorithm was also implemented.[19] For holmium(III)-based molecules, the electronic-nuclear spin states were shown to undergo a clock transition (i.e., the level separations being insensitive to a magnetic field to first order)[20] and to be coherently controlled by distortion and an electric field.[21] For europium(III)-based molecules, the nuclear spin states were optically initialized and controlled.[22]

Although electronic-nuclear or nuclear spin states are less susceptible to environment than electronic spin states, control and gate operations of the former are much slower than those of the latter. It is known that $4f$ orbitals of Ln-based molecules are typically highly localized well below the highest occupied molecular orbital, which hinders optical excitations of electronic states. Therefore, there may be a higher probability to find optically accessible molecules from TM-based molecular families,[23–25] as far as electronic spin states are targeted. Along this line, a molecular analogue closest to the NV^- center was discovered in a $Cr(IV)(aryl)_4$ family.[25] The experiment[25] showed that the electronic ground state of the $Cr(IV)(aryl)_4$ molecules has a spin $S = 1$ (triplet) with a small zero-field splitting (ZFS) and that the electronic first excited state has a spin $S = 0$ (singlet), which is the same as that of the NV^- center in diamond. The molecular electronic states were optically initialized, read-out and coherently controlled with microwaves.[25] Furthermore, ZFS parameters were shown to vary with modifications of ligands in the family,[25,26] although the sign of ZFS parameter D was not determined in the experiments.

Despite this progress, quantitative computational insights into the systems would facilitate the design of molecular qubits with enhanced properties such as narrower zero-phonon line (ZPL), more efficient spin initialization (or larger optical spin polarization), reduced intermolecular interactions, longer spin-lattice relaxation time, and longer spin coherence times. Multireference nature of electronic excitations plays a key role in absorption and

emission properties, non-radiative transitions between the states, and ZFS (or magnetic anisotropy). An understanding of these properties under different chemical environment is crucial in increasing the optical spin polarization and elucidation and reduction of spin decoherence factors. So far, there have been no studies of these properties for the Cr(IV)(aryl)$_4$ family.

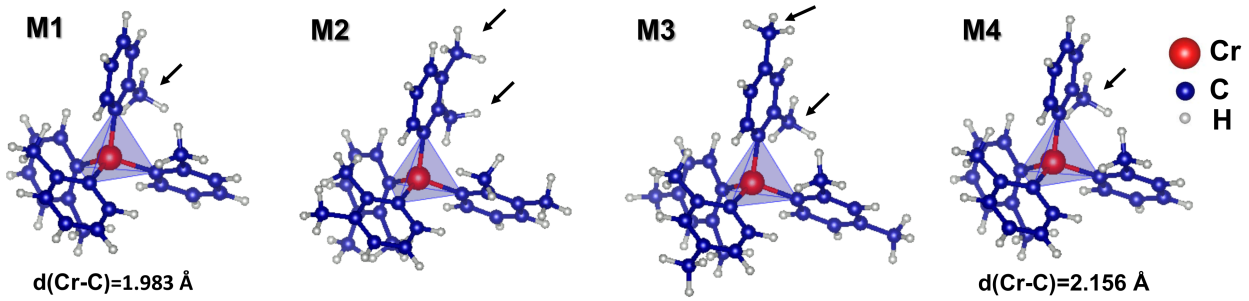

Figure 1: Atomic structures of four Cr(IV)(aryl)$_4$ molecules: **M1**, **M2**, **M3** and **M4**. Red, dark blue and grey circles denote Cr, C and H atoms, respectively. In each molecule, an approximately tetrahedral C cage containing the Cr atom is shown as a light blue polyhedron. **M4** has the same molecular symmetry as **M1**. In the experimental geometries, **M1** and **M4** have different bond lengths and bond angles (see Table 1 and main text for detail). Upon geometry relaxation, the atomic coordinates of **M4** become the same as those of **M1**.

In this work, we investigate multireference electronic excitations of several Cr(IV)(aryl)$_4$ molecules (aryl=o-tolyl (**M1**,**M4**), 2,3-dimethylphenyl **M2**, 2,4-dimethylphenyl (**M3**)), as shown in Fig. 1, using the multireference *ab initio* methods including spin-orbit coupling (SOC), and analyze the effect of different chemical environment on the excitations. Based on the calculated electronic spin-triplet and spin-singlet excitations, we study two SOC effects for the molecules such as (i) the ZFS of the ground spin-triplet state and (ii) transitions between spin-triplet and spin-singlet states (intersystem crossing, ISC), within the multireference *ab initio* formalism. Then we quantify hyperfine coupling to the ^{53}Cr nuclear spin and to the ^{1}H and ^{13}C nuclear spins of the ligands, and discuss their effects on decoherence of the molecular electronic spin states for the different molecules.

All four molecules consist of a Cr^{4+} ion in an approximately tetrahedral (T_d) environment produced by four surrounding carbohydrate ligand rings. Each ligand ring corresponds to

Table 1: Structural properties of all considered molecules (Fig. 1) where the atomic coordinates of **M1**, **M2**, and **M3** are taken from the experimental Cr(IV)(aryl)$_4$ molecular crystals,[25] while those of **M4** are from one of the experimental diluted molecular crystals with Sn replaced by Cr.[25]

Properties	**M1**	**M2**	**M3**	**M4**
Cr-C bond lengths (Å)	1.983	2.002, 2.017	1.990, 1.991 1.996, 1.998	2.156
C-Cr-C angle (degree)	113.07	109.55, 110.38	109.01, 109.34 109.72, 110.64	107.14
Molecular symmetry	S_4	C_2	C_1	S_4

the benzene molecule with one or two hydrogen atoms being replaced by a methyl group. The **M1**, **M2**, and **M3** molecules differ by number and/or positions of the methyl group in the ligand rings (marked as arrows in Fig. 1). Table 1 lists exact molecular symmetry and bond lengths and angles of the Cr ion and the four closest C sites for the molecules with the experimental geometries.[25] Note that both **M1** and **M4** molecules have exact S_4 symmetry but the Cr-C bond length differs by 0.173 Å. The atomic coordinates of the **M1**, **M2**, and **M3** molecules are taken from the experimental Cr(IV)(aryl)$_4$ molecular crystals, while those of the **M4** molecule are from one of the synthesized diluted molecular crystals with a Cr:Sn ratio of 0.75%.[25] In this diluted crystal, since only atomic coordinates of a Sn(IV)(aryl)$_4$ cluster were reported,[25] the **M4** molecule is constructed by replacing Sn by Cr in the Sn(IV) cluster. Thus, the **M4** molecular structure corresponds predominantly to the Sn(aryl)$_4$ geometry, and the calculations for the **M1** molecule (rather than for **M4**), therefore, better represent the experimental data for the S_4-symmetric Cr(IV)(o-tolyl)$_4$ molecule. Nevertheless, as discussed later, the results for the **M4** molecule are useful for an understanding of the relationship between ligand fields and structure. Therefore, we focus on **M1**, **M2**, and **M3** except for a study of the structural effect on ligand fields.

RESULTS AND DISCUSSION

Multireference Electronic Excitations

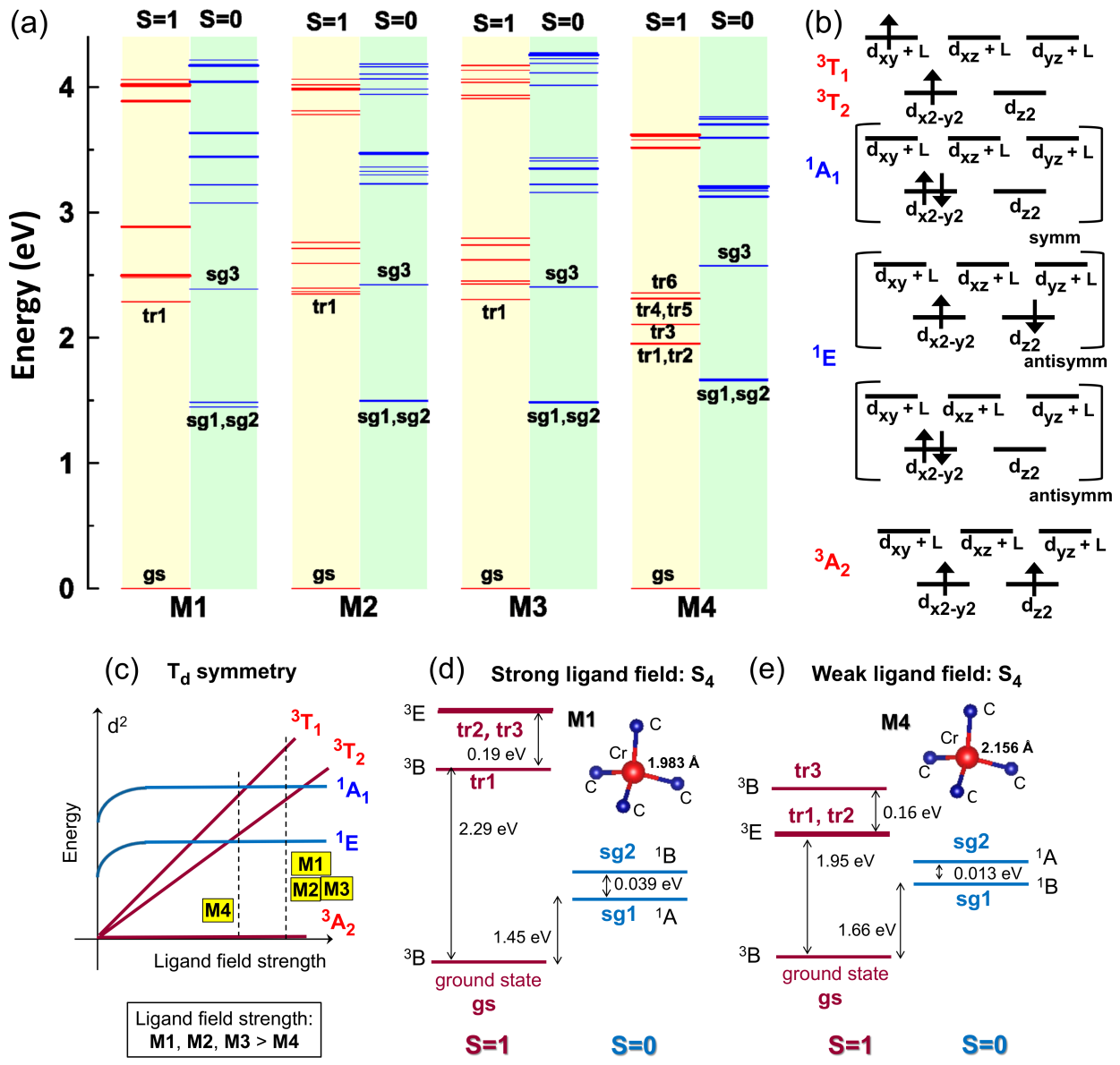

Figure 2: (a) Multireference electronic excitation energies of all considered molecules with the experimental structures without SOC. The ground state and first-excited $S = 1$ state are labeled as **gs** and **tr1**, respectively, while three lowest $S = 0$ states are labeled as **sg1**, **sg2** and **sg3**. Thicker lines indicate states with degeneracy. (b) Diagrams of low-lying state configurations under T_d symmetry, considering only Cr $3d$ orbitals, for simplicity (L: ligand orbitals), where **antisymm** and **symm** denote antisymmetric and symmetric combinations of two possible configurations. For example, one of the ^1E states is an antisymmetric combination of two electrons at either $d_{x^2-y^2}$ or d_{z^2} orbital. For $^3T_1$ and $^3T_2$, six configurations are possible from the diagrams. (c) Schematic Tanabe-Sugano diagram[27] of energy vs ligand-field strength for $3d^2$ systems under T_d symmetry. The lower molecular symmetries than T_d lift threefold degeneracy in $^3T_1$ and $^3T_2$ and twofold degeneracy in ^1E. For **M4**, **tr1**-**tr6** levels appear between **sg3** and **sg1**/**sg2** levels in energy. That is not the case for the others. (d)-(e) four spin-triplet and two spin-singlet states for **M1** and **M4**. The ordering of the excited spin-triplet (spin-singlet) states for **M4** is reversed to that for **M1**.

In order to include static and dynamic correlations into the electronic structure, we perform multireference *ab-initio* calculations, using the state-average complete active space self consistent field (SA-CASSCF) method[28,29] followed by the multi-state[30] second-order multireference perturbation theory correction (CASPT2),[31,32] as implemented in the `Molcas/Openmolcas` codes.[33,34] The active space consists of 10 electrons and 12 molecular orbitals. A computational detail is described in Methods section.

Figure 2(a) shows our calculated SA-CASSCF+CASPT2 energies of spin-triplet and spin-singlet states without SOC for all considered molecules with the experimental atomic structures taken from Ref.[25] In all cases, we observe the following features: (i) the ground state, **gs**, is a spin-triplet ($S = 1$) well separated in energy from the first-excited spin-triplet state, **tr1**; (ii) the first excited state, **sg1**, is a spin-singlet ($S = 0$) almost degenerate with the next spin-singlet state, **sg2**. Our calculated low-lying spin-triplet and spin-singlet energies are listed in Table S4 of the SI.

Figure 2(b) presents diagrams of a few low-lying state configurations under exact T_d symmetry, for simplicity, considering only Cr $3d$ orbitals, where **L** stands for ligand $2p$ orbitals hybridized with Cr t_{2g} orbitals. Under exact T_d symmetry, the ground state, $^3A_2$, consists of nominally singly-occupied lower-energy e_g orbitals and nominally empty higher-energy t_{2g} orbitals hybridized with ligand p orbitals. For strong ligand fields, the ligand field theory[27] dictates that the first- and second-excited states are spin-singlet states with ^1E and $^1A_1$ characters, respectively (Fig. 2(b),(c)). For **M1**, since the symmetry is lowered to S_4, the ground state has now a character of ^3B, while the degenerate lowest spin-singlet states are split into ^1A and ^1B states (Fig. 2(d)). The bottom and top diagrams of the ^1E state shown in Fig. 2(b) correspond to the ^1A and ^1B states, respectively. The $^3T_2$ state under T_d symmetry is also split into ^3B and ^3E characters under S_4 symmetry. Interestingly, for **M4** (with S_4 symmetry), all six lowest excited triplet states, **tr1**-**tr6**, that correspond to two threefold degenerate states ($^3T_2$, $^3T_1$) under T_d symmetry, appear between the excited spin-singlet state **sg3** and the almost degenerate singlet states **sg1**/**sg2** in energy. However, that

is not the case for the other molecules (Fig. 2(a)). The Tanabe-Sugano diagram (Fig. 2(c)) indicates that **M4** has a weaker ligand field than the rest of the molecules, which is consistent with the Cr-C bond length being significantly larger for **M4**. We also find that different ligand-field strengths affect the ordering of the excited spin-triplet states (^3B and ^3E) as well as that of the excited spin-singlet states (^1A and ^1B) for **M1** and **M4**. Both orderings are reversed in the two molecules (Fig. 2(d),(e)).

Table 2: Calculated vertical excitation (VE) energies ΔE_{VE} between the ground spin-triplet state (**gs**) and the lowest spin-singlet state (**sg1** in Fig. 2) as well as ZPL energies ΔE_{ZPL} of all considered molecules (see the main text for detail).

Properties	**M1**	**M2**	**M3**	**M4**
ΔE_{VE} (eV)	1.448	1.493	1.483	1.658
ΔE_{ZPL} (eV)	1.415	1.436	1.419	N/A
ΔE_{ZPL} (eV) (Exp. 25)	1.210	1.229	1.210	N/A

We extract a vertical excitation (VE) energy for each molecule from an energy difference between the ground state and the lowest spin-singlet state (Fig. 2(a)) obtained from the experimental geometry. Our calculations show that the VE energies for **M1**, **M2**, and **M3** are close to each other, in the range of 1.448-1.493 eV, while the VE energy of **M4** is somewhat higher (Table 2). The reason that the VE energy of **M4** is an outlier compared to those of the other molecules may be related to the substantially larger Cr-C bond length of **M4**. We also compute a ZPL energy by subtracting a SA-CASSCF+CASPT2 energy of the ground spin-triplet state using a DFT-relaxed geometry with $S = 1$ from that of the lowest spin-singlet state using a separate DFT-relaxed geometry with $S = 0$ (see Methods section for detail). Upon the geometry relaxation, we observe large structural changes only in the **M4** molecule. As a result, the relaxed atomic coordinates of **M4** become essentially identical to those of **M1**. Henceforth, we investigate properties of **M1**, **M2**, and **M3** only. We find that the ZPL energy of each molecule is smaller by < 0.1 eV than the VE energy (Table 2). The calculated ZPL energies of the considered molecules are slightly higher than the experimental ZPL energies which are in the range of 1.210-1.229 eV.[25] These small deviations from the

experimental energies are typical for SA-CASSCF+CASPT2 calculations due to approximate treatment of dynamical correlations.[35,36]

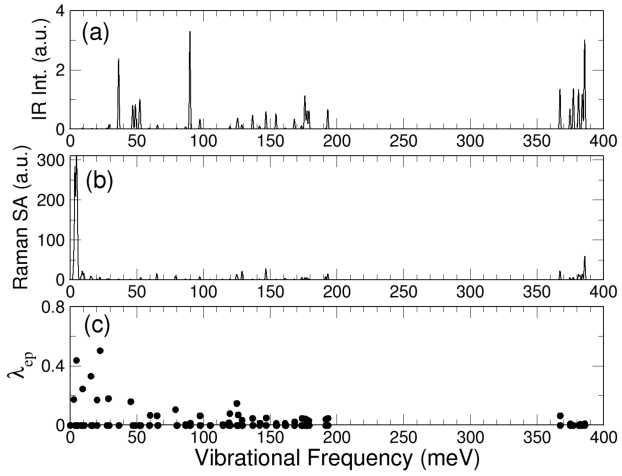

Figure 3: (a) Infrared intensity (in units of (Debye/Å)^2) and (b) Raman scattering activity (in units of Å^4/amu) of the vibrational modes for **M1** which are computed using DFT. (c) Calculated dimensionless vibronic coupling strength of the vibrational modes for the ground spin-triplet state of **M1**.

Since the difference between the VE and ZPL energies is small (Table 2), it is likely that electron-phonon coupling (i.e., vibronic coupling) may be small for the ground spin-triplet state and lowest spin-singlet state of the **M1**, **M2**, and **M3** molecules. As a representative, we compute vibrational modes and vibronic coupling for the ground spin-triplet state of **M1**, using the DFT code `NRLMOL`.[37–39] As shown in Fig. 3, the vibrational modes have a range of 2.8 meV to 386 meV. We also calculate dimensionless vibronic coupling $\lambda_{\rm ep}$ of each vibrational mode using the method described in Ref. 40. We find that only 10 vibrational modes (2.8-124.8 meV) with A symmetry have intermediate dimensionless vibronic coupling strength ($0.1 < \lambda_{\rm ep} < 0.5$), while the rest of the modes have much smaller or zero vibronic coupling. This result is consistent with our result that the VE and ZPL energies differ by less than 0.1 eV.

Spin-Orbit Coupling Effect I: Zero-Field Splitting

All the electronic spin-triplet states shown in Fig. 2 are split by SOC and/or dipolar

Table 3: Calculated zero-field splitting or magnetic anisotropy parameters D and E (in GHz) as well as **g** tensor of the ground spin-triplet state for all considered molecules with the experimental geometries, compared to experimental data from Ref.[25] The experimental **g** tensor is isotropic and it is 1.985 for the **M1**, **M2**, and **M3** molecules. The theoretical D, E, and **g** tensor are from the RASSI-SO-CASPT2 calculations with 13 spin-triplet and 15 spin-singlet states.

Properties	**M1**	**M2**	**M3**
D	−5.7	−3.3	−2.4
E	0.0	0.7	0.3
$\lvert E/D\rvert$	0.0	0.21	0.13
$\lvert D\rvert$ (Exp. 25)	3.63	1.83	4.11
$\lvert E\rvert$ (Exp. 25)	0.00	0.49	0.54
$\lvert E/D\rvert$	0.0	0.27	0.13
g_{xx}	1.983	1.979	1.983
g_{yy}	1.983	1.980	1.981
g_{zz}	1.977	1.982	1.978

electron spin-spin coupling (SSC). In this work, we mostly focus on the level splitting of the ground spin-triplet state (non-degenerate) which can be described by the following ZFS Hamiltonian:

$$\hat{H}_{\text{eff}} = D\hat{S}_z^2 - \frac{1}{3}DS(S+1) + E\big(\hat{S}_x^2 - \hat{S}_y^2\big). \tag{1}$$

Here D and E are uniaxial and transverse (rhombic) ZFS (or magnetic anisotropy) parameters, and $\hat{\mathbf{S}}$ is the pseudospin operator with $S = 1$. The coordinate system corresponds to the molecular anisotropy axes. For $S = 1$, the eigenvalues of the ZFS Hamiltonian are $D + E$, $D - E$, and 0.

We first investigate a SSC contribution to the ZFS parameters of the ground spin-triplet state for the **M1** molecule with the experimental geometry, by performing multireference calculations using the `ORCA` code.[41] The SSC contribution turns out to be negligible ($|D_{\text{SSC}}|$ <0.01cm^{-1}, $E_{\text{SSC}} = 0$). As expected, since the SSC contribution is a first-order effect, it was shown that the contribution was mainly determined by the ground state rather than excited states, and that it was not sensitive to the active space size, the number of roots for state average, and inclusion of dynamic correlations.[42] Therefore, we expect that

the SSC contributions for the other molecules are also negligible and that the experimental ZFS parameters originate entirely from SOC.

Since the ground spin-triplet state is orbitally non-degenerate, it is split by second-order SOC, which depends on the excited states. We compute SOC contributions to the D and E parameters of the ground spin-triplet state for all considered molecules with the experimental atomic coordinates, considering 13 spin-triplet and 15 spin-singlet states for each molecule (see Methods section for detail). As listed in Table 3, for the **M1** molecule, the calculated E parameter is zero, which reflects S_4 symmetry. The magnitude of the calculated D parameter of **M1** is comparable to the experimental value,[25] while those of **M2** and **M3** are somewhat overestimated and underestimated than the experimental values,[25] respectively. Interestingly, the calculated $|E/D|$ ratios for **M1**, **M2**, and **M3** agree well with the experimental data, which suggests that the active spaces retain the molecular symmetries. The small discrepancies between the calculated and the experimental ZFS parameters may be attributed to (i) atomic structures that could slightly differ from experimental systems and (ii) approximate treatment of dynamical correlations which influences the excited-state wavefunctions and energies. Since the calculated D and E parameters in Table 3 arise from the second-order SOC effect, they depend on high-energy spin-singlet states as well as spin-triplet states. Importantly, SOC contributions to D and E from different excited states have different magnitudes and different signs (see Tables S5-S7 in the SI). (The configurations of all roots for **M1** are listed in Tables S8-S9 in the SI.) As a result, the values of the ZFS parameters are, to a large degree, determined by high-energy multireference excited states that can be substantially modified by slight changes of ligands. The ZFS parameter values are, therefore, expected to be sensitive to small perturbations or atomic structure variations. This is consistent with experimental and theoretical findings that the D and E parameters noticeably vary among the **M1**, **M2**, and **M3** molecules.

Furthermore, we find that the signs of the calculated D parameters are *negative* for all considered molecules. This indicates that the lowest magnetic sub-levels are degenerate

$M_s = \pm 1$ states for $E = 0$, or linear combinations of $M_s = \pm 1$ states for $E \neq 0$. While the sign of the D parameter was *not* determined in the experimental studies,[25,26] it can be unambiguously obtained by specific heat measurements as a function of temperature.[43]

For the **M1** molecule, the magnetic easy axis is found to be along the S_4 symmetry axis. Anisotropy in the calculated **g** tensor (Table 3) corroborates the magnetic anisotropy or non-zero ZFS parameters. The principal values of the calculated **g** tensor agree with the experimental values, although the latter values were assumed to be isotropic in fitting of the experimental electron paramagnetic resonance spectra.[25]

We also briefly discuss ZFS of the first excited non-degenerate spin-triplet state since its spin sub-levels M_s' are involved in ISC, as discussed in the next section. Regarding the first excited spin-triple state, we consider only the second-order SOC contribution to its ZFS parameters which are labeled as D' and E' in order to distinguish from those of the ground state. Following the same procedure as above, we find that for the **M1** and **M3** molecules, the D' parameter is negative, while for the **M2** molecule, it is positive. Similarly to the case of the ground spin-triplet state, the **M2** and **M3** molecules have a nonzero E' parameter, while it vanishes for the **M1** molecule. Compared to the ground spin-triplet state, the splitting of the sub-levels is much larger. For the three molecules, the $|D'|$ value ranges from 72.8 to 91.7 GHz (2.43-3.06 cm^{-1}), while the nonzero E' value ranges from 5.1 to 20.7 GHz (0.17-0.69 cm^{-1}).

Spin-Orbit Coupling Effect II: Intersystem Crossing

In addition to the level splitting, SOC allows for radiative and non-radiative transitions between spin-triplet and spin-singlet states. Such transitions plays an important role in achieving an optical spin interface. In particular, in Ref. 25 it was proposed that an optical spin initialization for the considered Cr(IV)(aryl)$_4$ molecules can be realized by applying a resonant light with frequency equal to the energy difference between the lowest singlet state **sg1** and one of the sub-levels of the spin-triplet ground state. The molecule in this ('bright')

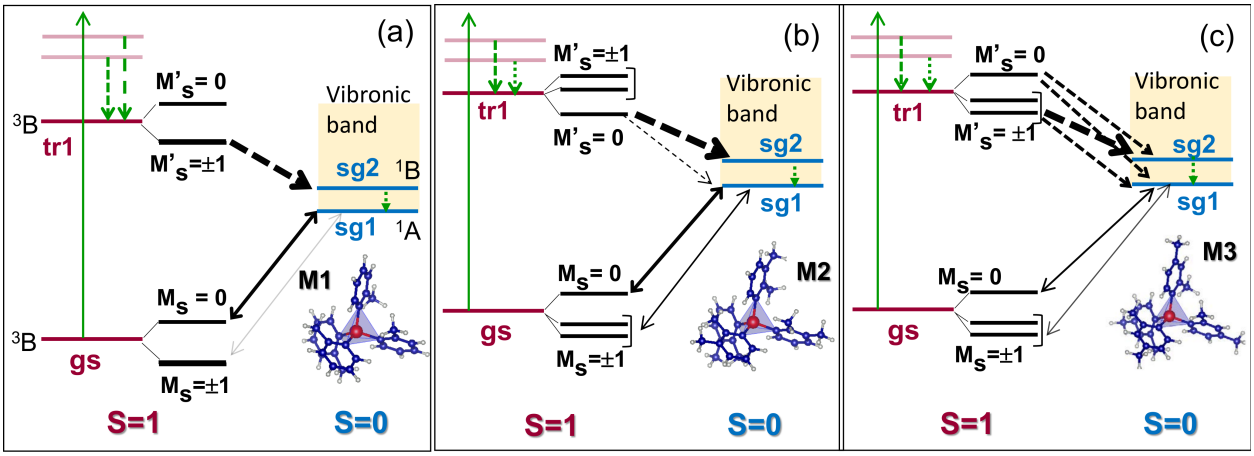

Figure 4: Diagrams of radiative (solid arrows) and non-radiative (dashed arrows) relaxation/absorption processes for (a) **M1**, (b) **M2**, and (c) **M3**. Spin-conserving (spin-flip) processes are shown as green (black) arrows. Thicknesses of black dashed arrows represent magnitudes of the SOC matrix elements, while thicknesses of black solid arrows denotes magnitudes of the oscillator strengths. The green solid up-arrow indicates off-resonant excitation. Due to fast internal conversion from **sg2** and **sg1**, radiative transitions between **sg2** and the M_s sub-levels of **gs** are not shown. Shaded areas in the spin-singlet states, **sg1** and **sg2**, represent vibronic bands. In the case of off-resonant excitation, the predominant radiative relaxation from **sg1** to the $M_s = 0$ sub-level of **gs** renders the spin initialization into the $M_s = 0$ sub-level of **gs**, for all considered molecules.

spin sub-level is then more likely to be excited into **sg1** than if it is in other ('dark') spin sub-levels (assuming that the line broadening is smaller than the sub-level separation). On the other hand, the molecule in **sg1** can decay into any of the ground triplet spin sub-levels with comparable rates, producing the photoluminescence. Since the lifetime of **sg1** is much smaller than the spin-lattice relaxation time for the ground triplet state,[25] during optical cycles, these processes would eventually transfer the molecule from the 'bright' spin sub-level to the 'dark' spin sub-level(s). Such depopulation of the 'bright' spin sub-level was demonstrated experimentally for the **M1** molecule that was reflected in a 14% reduction of the observed photoluminescence.[25]

Our calculations provide additional insight into this process by evaluating absorption and emission rates between the spin-singlet states and the ground spin-triplet sub-levels M_s. We find that the decay rates from **sg1** to the different M_s sub-levels of **gs** are not always the same. In particular, for the S_4-symmetric **M1** molecule, a radiative transition occurs

predominantly between the $M_s = 0$ sub-level and **sg1** (denoted as a thick solid black arrow in Fig. 4(a)), while the $M_s = \pm 1$ levels have radiative transitions primarily with **sg2** (not shown). If the **M1** molecule is excited from the lowest spin-triplet sub-levels $M_s = \pm 1$ to **sg2** by a light with a resonant frequency, then instead of a radiative decay back to the $M_s = \pm 1$ sub-levels, the molecule undergoes non-radiative internal conversion from **sg2** to **sg1** (denoted as a tiny dashed green arrow in Fig. 4(a)) and a subsequent radiative decay from **sg1** to the $M_s = 0$ sub-level, since the internal conversion rate is much larger than the radiative decay rate. During optical cycles, the $M_s = \pm 1$ sub-levels become depopulated and the molecule is initialized to have $M_s = 0$. The same mechanism is applied to the **M2** and **M3** molecules (Fig. 4(b),(c)). As the molecular symmetry is lowered, the ratio between the radiative decay to the $M_s = 0$ sub-level and that to the $M_s = \pm 1$ sub-levels greatly decreases, and therefore the efficiency in the optically-induced spin initialization decreases. Based on this, we expect that the efficiency in the optical spin initialization is largest for **M1** and smallest for **M3**.

For point defects in wide bandgap semiconductors, an optical spin interface is realized using a different approach that utilizes non-radiative ISC transitions.[44–47] Our results indicate that a similar technique may be used to achieve optical spin initialization in the Cr(IV)(aryl)$_4$ molecules which would be an alternative to the method used in Ref. 25. First, a non-resonant light is used to excite the molecules into higher-lying spin-triplet states (see full green arrows in Fig. 4), which is followed by rapid non-radiative internal conversion to **tr1** (dashed green arrows in Fig. 4). In principle, spontaneous emissions from **tr1** to **gs** can then occur. Our estimation, however, shows that a spontaneous emission rate from a higher-energy spin-triplet state to **gs** is at most $\sim 10^6$ s^{-1}. Since this rate is much smaller than typical non-radiative ISC rates in TM-based molecules, $\sim 10^{12}$ s^{-1},[23,48,49] the radiative decay from the higher-lying spin-triplet states to **gs** is unlikely to be observed. Instead, the molecules undergo non-radiative ISC from the M_s' sub-levels of **tr1** to either **sg1** or **sg2**. This ISC transition involves phonon emission when the energy of **tr1** falls within the phonon

or vibronic energy range of **sg1**/**sg2** (shaded areas in Fig. 4). The relative importance of the non-radiative ISC transition rates is estimated by comparing the SOC matrix elements between the M_s' sub-levels of **tr1** and the spin-singlet states. As shown in Fig. 4, non-radiative ISC transition rates (denoted as black dashed arrows) strongly depend on both characters of the sub-levels M_s' of **tr1** and the ligand type. For example, for the **M1** molecule, the ISC transition occurs predominantly between the $M_s' = \pm 1$ levels of **tr1** and **sg2**. Such a M_s'-selective ISC rate plays a crucial role in establishing the spin initialization in the NV^- center and similar systems[44–47] because the spontaneous emission rate from **tr1** to **gs** is comparable to the ISC rate. In order to realize such a mechanism within molecules, substantial reduction of the ISC rate is required.[49,50] For the considered $Cr(IV)(aryl)_4$ molecules, the M_s'-selective ISC rate, however, does not affect the spin initialization. Nevertheless, the spin initialization can be potentially achieved here due to the M_s-selective phosphorescence discussed above. Indeed, the dominant pathway involves internal conversion to **sg1** and then primarily radiative relaxation to M_s=0 of **gs**, which under optical cycles results in transfer of population from $M_s = \pm 1$ to $M_s = 0$ for all considered molecules. Importantly, the efficiency of this process can be improved by ligand manipulations since the M_s-selectivity of phosphorescence highly depends on ligands.

Spin Decoherence: Effects of Hyperfine Coupling

The molecular electronic spin states are susceptible to various sources of spin decoherence arising from environment[51] even at low temperatures. In molecular crystals, electron-phonon (and spin-phonon) interactions are known to be critical for electron spin relaxation time T_1 which limits electron spin coherence time T_2. The latter time was shown to increase by lowering the concentration of Cr(IV)-based molecules in diluted molecular crystals,[26] suggesting that dipolar electron spin-spin interactions between different Cr(IV)-based molecules play an important role in spin decoherence. At the single molecule level, the ^{53}Cr nuclear spin and ^{13}C and ^{1}H nuclear spins of the ligands interact with the molecular electronic spin. These

Table 4: Isotropic Fermi contact $\mathbf{A}_{\mathrm{FC}}^{\mathrm{Cr}}$ and principal values of spin-dipole contributions $A_{\mathrm{SD,i}}^{\mathrm{Cr}}$ ($i = 1, 2, 3$) of the ^{53}Cr hyperfine matrix as well as the ^{53}Cr nuclear quadrupole tensor $\mathbf{P}^{\mathrm{Cr}}$ of the electronic ground state for all considered molecules. The coordinate system corresponds to the molecular magnetic anisotropy axes. Units of all values are MHz. For simplicity, we drop "Cr" in symbols below.

Properties	**M1**	**M2**	**M3**
A_{FC}	94.9	95.8	95.4
$A_{\mathrm{SD},1}$	−0.27	0.4	0.3
$A_{\mathrm{SD},2}$	0.14	−0.4	−0.3
$A_{\mathrm{SD},3}$	0.14	0.0	0.0
P_{xx}	−1.5	0.8	−0.5
P_{xy}	0.0	0.2	−0.1
P_{xz}	0.0	0.7	−0.3
P_{yy}	−1.5	0.4	−0.4
P_{yz}	0.0	0.2	0.0
P_{zz}	3.0	−0.4	0.9

hyperfine and superhyperfine interactions can influence the phase of the molecular spin state. Furthermore, nuclear spin-spin interactions can flip-flop the nuclear spin states, indirectly affecting the molecular electronic spin state as dynamic processes.[16,52,53] In this work, we focus on quantification of the hyperfine and superhyperfine interactions and their effects on the M_s sub-levels of the electronic ground state under different chemical environment by considering the **M1**, **M2**, and **M3** molecules.

Since we are interested in the hyperfine and superhyperfine interactions of the electronic ground spin-triplet state, we use the CASSCF(10,12) wavefunctions obtained from the state average over one root. The interaction between the molecular electronic spin and the nuclear spins is described by the following effective spin Hamiltonian

$$\hat{H}_{\mathrm{HF}} = \hat{\mathbf{S}} \cdot \mathbf{A}_{\mathrm{Cr}} \cdot \hat{\mathbf{I}}_{\mathrm{Cr}} + \hat{\mathbf{I}}_{\mathrm{Cr}} \cdot \mathbf{P}_{\mathrm{Cr}} \cdot \hat{\mathbf{I}}_{\mathrm{Cr}} + \sum_{i=\mathrm{all}\ ^{1}\mathrm{H},^{13}\mathrm{C}} \hat{\mathbf{S}} \cdot \mathbf{A}_i \cdot \hat{\mathbf{I}}_i. \tag{2}$$

The first term is the magnetic hyperfine interaction between the electronic pseudospin $\hat{\mathbf{S}}$ and the ^{53}Cr nuclear spin $\hat{\mathbf{I}}_{\mathrm{Cr}}$ =3/2. The natural abundance of ^{53}Cr is 9.501%. The second term describes the ^{53}Cr nuclear quadrupole interaction which is proportional to the electric-field

gradient at the nuclear site. The nuclear quadruple interaction exists for any non-spherical nucleus with spin larger than 1/2. The third term describes the superhyperfine interaction of the pseudospin with the nuclear spins in the ligands, i.e., with ^{1}H spins $I_{\rm H}$ =3/2 and with ^{13}C spins $I_{\rm C}$ =1/2. The natural abundances of ^{13}C and ^{1}H are 1.07% and 99.9885%, respectively. The summation runs over all ^{13}C and ^{1}H atoms in the ligands.

We discuss quantification of the ^{53}Cr hyperfine interaction. Table 4 lists the calculated ^{53}Cr hyperfine matrix $\mathbf{A}_{\rm Cr}$ for all considered molecules. The ^{53}Cr hyperfine coupling primarily originates from the Fermi contact term that ranges from 94.9 to 95.8 MHz for the three molecules. This term comes from significant spin density at the Cr nuclear site, which is caused by hybridization between unpaired Cr 4s and 3d orbitals. The spin-dipole contribution to the hyperfine coupling is less than 1% of the Fermi contact term. The paramagnetic spin orbital (PSO) contribution is absent. We find that the signs of the hyperfine matrix elements are positive from a separate DFT calculation of the hyperfine matrix within the local density approximation[54] for the exchange-correlation functional without self-interaction correction using the `FLOSIC` code[55,56] (where the same basis sets as those of `NRLMOL` are used). For all considered molecules, the elements of the ^{53}Cr nuclear quadrupole tensor $\mathbf{P}_{\rm Cr}$ turn out to be very small (0.1-1.5 MHz) and they reflect the molecular symmetries.

The superhyperfine interactions of all the ^{1}H nuclear spins mainly arise from the spin-dipole contribution which obeys the power law as a function of the nuclear distance R from the Cr ion, as shown in Fig. 5(a). In this plot, $|A^{\rm H}_{\rm dip}|$ is defined to be $|A^{\rm H}_{\rm dip,1}-(A^{\rm H}_{\rm dip,2}+A^{\rm H}_{\rm dip,3})/2|$, where $A^{\rm H}_{\rm dip,i}$ (i =1,2,3) are three principal values of the spin-dipole contribution matrix to $\mathbf{A}_{\rm H}$. Here $A^{\rm H}_{\rm dip,1}$ is set to be the largest-magnitude principal value. We observe that $A^{\rm H}_{\rm dip,2}$ is similar to $A^{\rm H}_{\rm dip,3}$. We find that the superhyperfine interactions of the ^{13}C nuclear spins are more complex than the ^{1}H isotope case, showing the following two features. Firstly, there is non-negligible spin density at the four nearest neighboring C sites. If these four C sites have nuclear spins, the dominant contributions come from the Fermi contact term of 34-35 MHz (Fig. 5(b)). Since the Fermi contact term decays exponentially with the

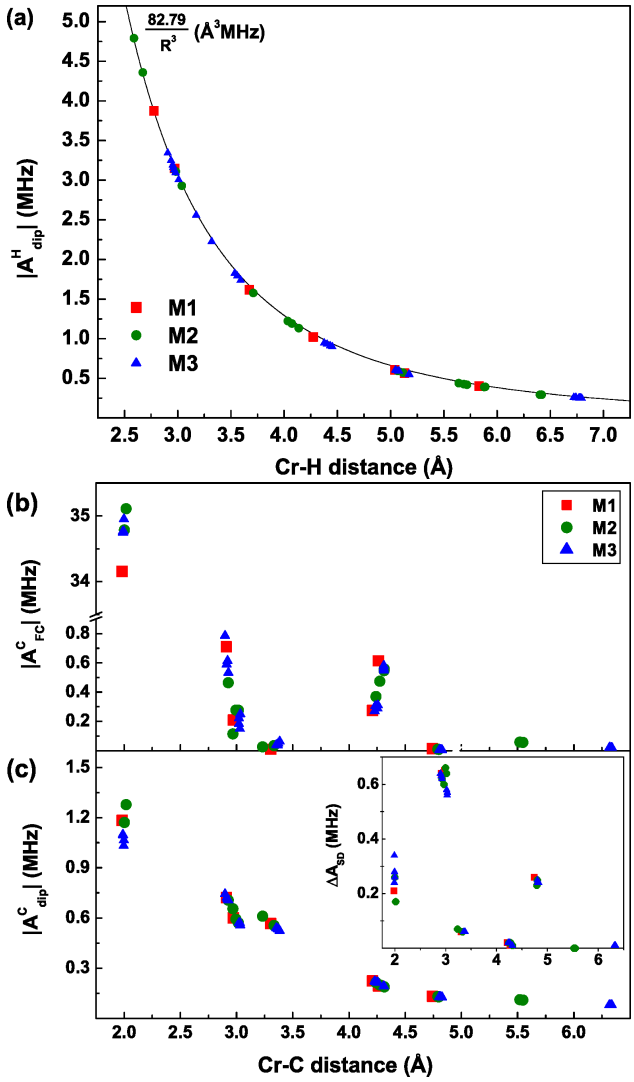

Figure 5: (a) Spin-dipolar contributions to the superhyperfine matrix for the ^{1}H nuclei as a function of the distance from the Cr ion for all considered molecules. (b) Fermi contact and (c) spin-dipolar contributions to the superhyperfine matrix for the ^{13}C nuclei as a function of the distance from the Cr ion for all considered molecules. $|A^{\mathrm{H,C}}_{\mathrm{dip}}|$ are defined to be $|A^{\mathrm{H,C}}_{\mathrm{dip},1} - (A^{\mathrm{H,C}}_{\mathrm{dip},2} + A^{\mathrm{H,C}}_{\mathrm{dip},3})/2|$, where $A^{\mathrm{H,C}}_{\mathrm{dip,i}}$ (i=1,2,3) are three principal values of the spin-dipole contribution matrix to $\mathbf{A}_{\mathrm{H,C}}$, and $A^{\mathrm{H,C}}_{\mathrm{dip},1}$ is the largest-magnitude principal value. In the inset of (c), ΔA_{SD} is defined to be $|A^{\mathrm{C}}_{\mathrm{dip},2} - A^{\mathrm{H}}_{\mathrm{dip},3}|$.

distance from the nuclear site, for the ^{13}C sites at intermediate distances from the Cr site, the superhyperfine interactions have contributions from both the Fermi contact and spin-dipole terms (Fig. 5(c)). Secondly, for the ^{13}C sites far from the Cr site, although the spin-dipole contributions outweigh the Fermi contact terms, they do not follow the usual power law, $1/R^3$, and there are nonzero differences between $A^{\mathrm{C}}_{\mathrm{dip},2}$ and $A^{\mathrm{C}}_{\mathrm{dip},3}$.

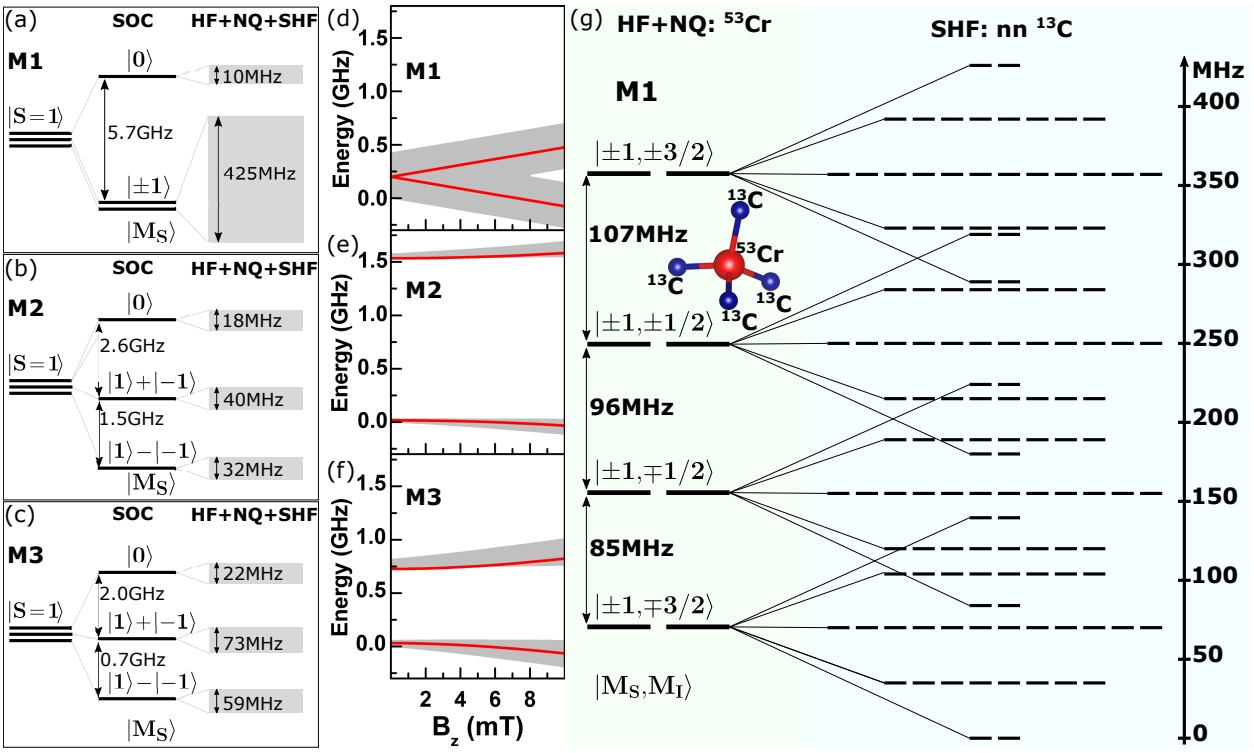

Figure 6: (a)-(c) Diagrams of the sub-level splitting of the electronic ground spin-triplet state due to the SOC, hyperfine (HF) and nuclear quadruple (NQ) coupling with the ^{53}Cr nucleus, and superhyperfine (SHF) coupling to the four nearest-neighboring (nn) ^{13}C nuclei. Grey bands represent the range of electronic-nuclear levels formed by the HF, NQ and SHF interactions. (d)-(f) Dependencies of the M_s sub-levels (red lines) and the ranges of HF+NQ+SHF levels (gray bands) on an external magnetic field along the magnetic easy axis (z axis). (g) Detailed level splitting of the $|M_s = \pm 1\rangle$ doublet (of the ground spin-triplet state) for **M1** (zoom-in of (a)) where the non-equidistant electronic-nuclear levels $|M_s, M_I\rangle$ arise from non-zero nuclear quadrupole tensor of the ^{53}Cr nuclear spin. The rightmost energy levels are obtained when we include the superhyperfine coupling with the four ^{13}C nuclear spins closest to the ^{53}Cr site.

Now we discuss splitting of the M_s sub-levels of the electronic ground state considering the hyperfine and superhyperfine interactions for **M1**, **M2**, and **M3**. Regarding the superhyperfine interactions, we consider a simplified upper-bound case that all four C sites closest to the ^{53}Cr ion have nuclear spins, although this scenario may unlikely be realized in experiments. The level splitting induced by the ^{53}Cr hyperfine and such superhyperfine interactions, however, can provide an upper limit in the M_s sub-level splitting (or broadening). For molecular crystals without isotope purification, the ^{1}H superhyperfine interactions primarily affect electron spin decoherence since ^{1}H isotope has much higher natural abundance

than ^{53}Cr and ^{13}C isotopes.

We first present the level splitting of the **M1** molecule. Figure 6(a) and (g) show the splitting of the sub-levels of the electronic ground state for this molecule. Since the zero-field split energy for **M1**, 5.7 GHz, is much larger than the ^{53}Cr hyperfine interaction energy ($\sim$100 MHz), the $M_s = 0$ sub-level is well separated from the hyperfine splitting of the $M_s = \pm 1$ sub-levels. Thus, as long as the lowest degenerate $M_s = \pm 1$ doublet is concerned, the **M1** molecule behaves like an effective-spin $S_{\text{eff}} = \frac{1}{2}$ system. The positive signs of the hyperfine matrix elements suggest that the lowest energy levels are formed when the electronic and nuclear spin directions are antiparallel to each other such as $|M_s, M_I\rangle = |\pm 1, \mp 3/2\rangle$ levels, where M_I is the projection of the nuclear spin onto the magnetic easy axis. The small ^{53}Cr nuclear quadrupole interaction is predominantly responsible for non-equidistant spacing of the electronic-nuclear levels $|M_s, M_I\rangle$ (Fig. 6(g)). The consecutive electronic-nuclear level separation ranges from 85-107 MHz. With an addition of the superhyperfine coupling from the four nearest-neighboring ^{13}C nuclear spins, the $|M_s, M_I\rangle$ levels are further split in a complex fashion (rightmost column in Fig. 6(g)) and the overall broadening reaches about 425 MHz (lower shaded region in Fig. 6(a)). On the other hand, the $M_s = 0$ sub-level does not split much. The overall broadening from the hyperfine coupling, nuclear quadrupole, and superhyperfine coupling is only 10 MHz.

For the **M2** and **M3** molecules, the M_s sub-levels split into three levels with energies of $-|D| - E$, $-|D| + E$, and 0 due to the non-zero ZFS E parameter value. These three sub-levels further split due to the hyperfine and superhyperfine interactions. Their splitting is much smaller than that for the **M1** molecule. The overall broadening of the lowest and next-lowest energy sub-levels (or the width of the electronic-nuclear levels) for **M2** and **M3** reaches only several tens of MHz (Fig. 6(b),(c)) which is an order of magnitude smaller than that for the **M1** molecule. The sub-level broadening of **M2** is somewhat smaller than that for **M3**.

The above stark difference in the sub-level splitting between **M2** (or **M3**) and **M1** is

attributed to the fact that the two lowest zero-field split sub-levels of **M2** and **M3** are linear combinations of $M_s = +1$ and $M_s = -1$ sub-levels and so they are insensitive to an external magnetic field to first order, which represents a clock transition, while **M1** has the $M_s = \pm 1$ doublet. Compare the Zeeman diagrams of the two lowest M_s sub-levels for **M2** and **M3** with that for **M1** (see red lines in Fig. 6(d)-(f)). The hyperfine and superhyperfine interactions can be viewed as effective magnetic fields to the molecular electronic spin sub-levels. Therefore, the Zeeman energies associated with the effective fields enter as a higher-order effect for **M2** and **M3**, giving rise to very small splitting of the sub-levels. However, that is not the case for **M1**. Since the clock transition is induced by the ZFS E parameter for integer spins, the insensitivity to an external or effective magnetic field increases with increasing the E value. This also explains the somewhat smaller width of the electronic-nuclear levels for **M2** than for **M3** in Fig. 6(b) and (c). (For molecules with $S \geq 2$, higher-order transverse ZFS parameters can also induce a clock transition.) Next we study how the electronic-nuclear levels (including the hyperfine and superhyperfine interactions) evolve in the presence of an external magnetic field for **M1**, **M2**, and **M3**. The shaded regions in Fig. 6(d)-(f) show much larger splitting of the electronic-nuclear levels for **M1** than for **M2** and **M3**. It was shown that a clock transition with a large E value can suppress intermolecular interactions[43,57] for $S = 1$ molecules. Our results suggest that the effect of hyperfine and superhyperfine interactions on electron spin decoherence can be also greatly reduced by designing molecules with a large E value.

CONCLUSIONS

We investigate electronic spin-triplet and spin-singlet excitations and ZFS parameters of the ground spin-triplet state for a few Cr(IV)$(\text{aryl})_4$ molecules with slightly different ligands and different molecular symmetries, using multireference *ab-initio* methods. Our calculated ZPL energies are in agreement with the experimental data. We show that high-energy

spin-triplet and spin-singlet states play an important role in the ZFS parameters since SOC enters as a second-order effect and that SSC does not contribute to the ZFS parameters. The calculated ZFS parameters exhibit a significant dependence on ligands, which is consistent with the experimental data. We find that the uniaxial ZFS parameter of the ground state has a negative sign for all considered molecules. We suggest that the ISC mechanism can be used to achieve the optical spin initialization and that the efficiency of the spin initialization highly depends on ligand type. To acquire insight into electron spin decoherence, we calculate hyperfine interactions of the ^{53}Cr nuclear spin and ^{1}H and ^{13}C nuclear spins and study how these interactions induce the splitting of the electronic ground-state spin sub-levels. We show that the width of the sub-level splitting can be reduced by an order of magnitude when molecules have a significant ZFS E parameter value, compared to molecules with $E = 0$. We clarify that this effect is ascribed to a clock transition. Our findings suggest that by designing integer-spin molecules with a large E value (or transverse ZFS parameters), electron spin decoherence arising from hyperfine and superhyperfine interactions can be suppressed to a large degree.

COMPUTATIONAL METHODS

All computations are carried out at the single molecule level. Except for the calculations of the ZPL energies, experimental geometries from Ref. 25 are used. For the **M1**, **M2**, and **M3** molecules, we use atomic coordinates determined from the x-ray measurements on the corresponding molecular crystals.[25] For the **M4** molecule, the atomic positions obtained from measurements on the diluted molecular crystal formed by diluting Cr(IV)(o-tolyl)$_4$ molecules in their isostructural Sn analogs[25] are used. For all experimental structures, we adjust the C-H bond lengths to 1.09 Å. For the calculations of the ZPL energies, we relax the experimental geometries of the **M1**, **M2**, and **M3** molecules (in a gas phase) with fixed spins $S = 1$ and $S = 0$ separately, using the all-electron DFT code `NRLMOL`[37,38] with Gaussian-

orbital basis sets and very dense variational mesh under the Perdew-Burke-Ernzerhof (PBE) generalized gradient approximation (GGA)[58] for the exchange-correlation functional. The structures are relaxed without any symmetry constraints until the atomic forces are equal to or less than 0.005 eV/Å. The atomic coordinates of the relaxed geometries for **M1**, **M2**, and **M3** are listed in Table S1-S3 in the SI. The DFT-relaxed $S = 1$ and $S = 0$ geometries are used for the subsequent multireference calculations of the electronic excitations (see below).

The multireference *ab-initio* calculations are performed using the `Molcas/OpenMolcas` codes.[33,34] Scalar relativistic effects are included based on the second-order Douglas-Kroll-Hess Hamiltonian[59,60] and relativistically contracted all-electron correlation-consistent (cc) basis sets.[61,62] For the **M1** and **M4** molecules, we use polarized triple-ζ (cc-pVTZ-DK) contraction for the Cr atom and all C atoms, while we use polarized double-ζ (cc-pVDZ-DK) contraction for the H atoms. For the larger **M2** and **M3** molecules, the same basis sets are used except the C atoms from the methyl groups for which we use the cc-pVDZ-DK basis set. We confirm that the slightly smaller basis sets for **M2** and **M3** do not affect our results.

The electronic structure is calculated in three steps. First, in the absence of SOC, both for spin-triplet and spin-singlet states, the spin-free energies and eigenstates are obtained using the state-averaged complete active space self-consistent field (SA-CASSCF) method.[28,29] In the second step, the spin-free energies are further improved by including dynamic correlations, using the multi-state[30] second-order multireference perturbation theory (CASPT2).[31,32] These CASPT2-corrected spin-free energies are shown as electronic VE energies in Fig. 2(a). By applying the same multireference *ab-initio* methods to the DFT-relaxed geometries, we obtain the ZPL energies (see Table 2). Finally, in the third step, the SOC is included within the atomic mean-field approximation[63] using the restricted active space state interaction (RASSI)[64] method.

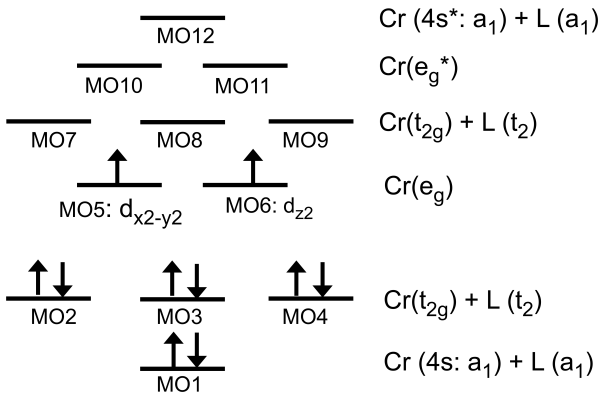

Figure 7: List of active molecular orbitals (MOs) used for the CASSCF(10,12) calculations for all considered molecules, where "L" stands for ligands. The configuration on the left hand side shows the ground spin-triplet state with nominal orbital occupancy. The active orbital images for the ground spin-triplet state for **M1** are shown in Fig. S1 in the SI.

In order to determine an optimal active space for the SA-CASSCF calculations, we start with a simple picture of Cr^{4+} ion with 2 active electrons in 5 active $3d$ orbitals. We use Cartesian axes along the axes of the cube in which the quasi-tetrahedral carbon cage (Fig. 1) is inscribed. In the tetrahedral symmetry, the d_{xy}, d_{xz}, and d_{yz} orbitals (MO7, MO8, MO9) strongly hybridize with three ligand orbitals (MO2, MO3, MO4). Therefore, these ligand orbitals and the corresponding 6 electrons (the ligand orbitals are nominally doubly occupied) are included in the active space. The $d_{x^2-y^2}$ and d_{z^2} orbitals (MO5, MO6) are non-bonding and they largely retain their atomic-like character. For a proper description of strong radial correlations for such localized orbitals, we add two (nominally empty) double-d-shell orbitals of the same spherical symmetry to the active space: $d^*_{x^2-y^2}$ and $d^*_{z^2}$ (MO10, MO11). Finally, the active space is supplemented by nominally empty Cr $4s$-like orbital (MO12) and the nominally doubly occupied ligand orbital (MO1) that hybridizes with the Cr $4s$-like orbital. Therefore, the active space consists of 10 electrons in 12 orbitals and we denote it as CAS(10,12). Figure 7 summarizes the active molecular orbitals and depicts the configuration of the ground spin-triplet state with nominal orbital occupancy. The active orbital images for the spin-triplet state of the **M1** molecule are shown in Fig. S1 in the SI. The number of roots in the SA-CASSCF(10,12) calculations is determined based on a significant energy gap

between root energies. We include 13 and 15 roots in the spin-triplet and spin-singlet states, respectively. The dominant configurations of the 13 spin-triplet roots and 15 spin-singlet roots for **M1** are listed in Table S8-S9 in the SI, respectively.

The multi-state CASPT2 calculations are done for all 13 (15) roots for the spin-triplet (spin-singlet) state using the default ionization potential-electron affinity (IPEA) shift (0.25 a.u.)[65] In order to improve the convergence, an additional real shift[66] of 0.3 a.u. is used in the CASPT2 calculations for all considered molecules. We check that our results are insensitive to the shift value.

The RASSI-SOC calculations are performed within the space spanned by 13 spin-triplet roots (including their spin sub-levels) and 15 spin-singlet roots using the SA-CASSCF wavefunctions and the multi-state CASPT2-corrected energies. The ZFS (or magnetic anisotropy) effective spin Hamiltonian as well as the **g** tensor are then constructed using the SINGLE_ANISO approach.[67]

The hyperfine coupling and superhyperfine coupling parameters are calculated using the method described in Ref. 68. Since we focus on the coupling parameters of the ground state, they are evaluated based on CASSCF(10,12) calculations for a single (ground spin-triplet) root. Correspondingly, RASSI-SOC calculations are done within the space spanned only by the three spin sub-levels of the ground spin-triplet using both CASSCF wavefunctions and energies. In this case, the CASPT2 step is skipped because it only affects the energy spacing between the roots.

The contribution of dipolar electron spin-spin interaction to the ZFS parameters for the **M1** molecule is calculated using the `ORCA` code.[41] We use cc-pVDZ-DK basis set for all atoms and CASSCF(8,8) calculations with MO2-MO9 as active orbitals for the ground spin-triplet state.

Acknowledgement

This work was funded by the Department of Energy (DOE) Basic Energy Sciences (BES) grant number DE-SC0018326. Computational support was provided by the Virginia Tech Advanced Research Center and the Extreme Science and Engineering Discovery Environment (XSEDE) under Project number DMR060009N which are supported by the National Science Foundation Grant number ACI-1548562. The authors are grateful to A. Karanovich for the hyperfine coupling calculation using the FLOSIC code.

Supporting Information Available

The Supporting Information is available free of charge.

DFT-relaxed atomic coordinates of the **M1**, **M2**, and **M3** molecules; SA-CASSCF+CASPT2 spin-free energies for all considered molecules; analysis of the ZFS parameters as a function of number of spin-triplet and spin-singlet roots for **M1**, **M2**, and **M3**; dominant configurations of the 13 spin-triplet and 15 spin-singlet roots for **M1**; images of the active orbitals for the spin-triplet SA-CASSCF(10,12) calculation for **M1** with SA natural occupancy.

References

(1) Awschalom, D. D.; Hanson, R.; Wrachtrup, J.; Zhou, B. B. Quantum technologies with optically interfaced solid-state spins. *Nat. Photonics* **2018**, *12*, 516–527.

(2) Hensen, B. et al. Loophole-free Bell inequality violation using electron spins separated by 1.3 kilometres. *Nature* **2015**, *526*, 682–686.

(3) Taminiau, T. H.; Cramer, J.; van der Sar, T.; Dobrovitski, V. V.; Hanson, R. Universal

control and error correction in multi-qubit spin registers in diamond. *Nat. Nanotechnol.* **2014**, *9*, 171–176.

(4) Epstein, R. J.; Mendoza, F. M.; Kato, Y. K.; Awschalom, D. D. Anisotropic interactions of a single spin and dark-spin spectroscopy in diamond. *Nat. Phys.* **2005**, *1*, 94–98.

(5) Balasubramanian, G.; Chan, I. Y.; Kolesov, R.; Al-Hmoud, M.; Tisler, J.; Shin, C.; Kim, C.; Wojcik, A.; Hemmer, P. R.; Krueger, A.; Hanke, T.; Leitenstorfer, A.; Bratschitsch, R.; Jelezko, F.; Wrachtrup, J. Nanoscale imaging magnetometry with diamond spins under ambient conditions. *Nature* **2008**, *455*, 648–651.

(6) Bassett, L. C.; Alkauskas, A.; Exarhos, A. L.; Fu, K.-M. C. Quantum defects by design. *Nanophotonics* **2019**, *8*, 1867 – 1888.

(7) Fuchs, G. D.; Dobrovitski, V. V.; Toyli, D. M.; Heremans, F. J.; Awschalom, D. D. Gigahertz Dynamics of a Strongly Driven Single Quantum Spin. *Science* **2009**, *326*, 1520–1522.

(8) He, Y.; Gorman, S. K.; Keith, D.; Kranz, L.; Keizer, J. G.; Simmons, M. Y. A two-qubit gate between phosphorus donor electrons in silicon. *Nature* **2019**, *571*, 371–375.

(9) Fricke, L.; Hile, S. J.; Kranz, L.; Chung, Y.; He, Y.; Pakkiam, P.; House, M. G.; Keizer, J. G.; Simmons, M. Y. Coherent control of a donor-molecule electron spin qubit in silicon. *Nat. Commun.* **2021**, *12*, 3323.

(10) Mądzik, M. T. et al. Precision tomography of a three-qubit donor quantum processor in silicon. *Nature* **2022**, *601*, 348–353.

(11) Davies, G.; Hamer, M. F.; Price, W. C. Optical studies of the 1.945 eV vibronic band in diamond. *Proc. R. Soc. Lond. A.: Math. Phys. Sci.* **1976**, *348*, 285–298.

(12) Rogers, L. J.; Armstrong, S.; Sellars, M. J.; Manson, N. B. Infrared emission of the NV centre in diamond: Zeeman and uniaxial stress studies. *New J. Phys.* **2008**, *10*, 103024.

(13) Batalov, A.; Zierl, C.; Gaebel, T.; Neumann, P.; Chan, I.-Y.; Balasubramanian, G.; Hemmer, P. R.; Jelezko, F.; Wrachtrup, J. Temporal Coherence of Photons Emitted by Single Nitrogen-Vacancy Defect Centers in Diamond Using Optical Rabi-Oscillations. *Phys. Rev. Lett.* **2008**, *100*, 077401.

(14) Kane, B. E. A silicon-based nuclear spin quantum computer. *Nature* **1998**, *393*, 133–137.

(15) Rugg, B. K.; Krzyaniak, M. D.; Phelan, B. T.; Ratner, M. A.; Young, R. M.; Wasielewski, M. R. Photodriven quantum teleportation of an electron spin state in a covalent donor-acceptor-radical system. *Nat. Chem.* **2019**, *11*, 981–986.

(16) Zadrozny, J. M.; Niklas, J.; Poluektov, O. G.; Freedman, D. E. Multiple Quantum Coherences from Hyperfine Transitions in a Vanadium(IV) Complex. *J. Am. Chem. Soc.* **2014**, *136*, 15841–15844.

(17) Atzori, M.; Morra, E.; Tesi, L.; Albino, A.; Chiesa, M.; Sorace, L.; Sessoli, R. Quantum Coherence Times Enhancement in Vanadium(IV)-based Potential Molecular Qubits: the Key Role of the Vanadyl Moiety. *J. Am. Chem. Soc.* **2016**, *138*, 11234–11244.

(18) Thiele, S.; Balestro, F.; Ballou, R.; Klyatskaya, S.; Ruben, M.; Wernsdorfer, W. Electrically Driven Nuclear Spin Resonance in Single-Molecule Magnets. *Science* **2014**, *344*, 1135–1138.

(19) Godfrin, C.; Ferhat, A.; Ballou, R.; Klyatskaya, S.; Ruben, M.; Wernsdorfer, W.; Balestro, F. Operating Quantum States in Single Magnetic Molecules: Implementation of Grover's Quantum Algorithm. *Phys. Rev. Lett.* **2017**, *119*, 187702.

(20) Shiddiq, M.; Komijani, D.; Duan, Y.; Gaita-Ariño, A.; Coronado, E.; Hill, S. Enhancing Coherence in Molecular Spin Qubits via Atomic Clock Transitions. *Nature* **2016**, *531*, 348–351.

(21) Liu, J.; Mrozek, J.; Ullah, A.; Duan, Y.; Baldoví, J. J.; Coronado, E.; Gaita-Ariño, A.; Ardavan, A. Quantum coherent spin-electric control in a molecular nanomagnet at clock transitions. *Nat. Phys.* **2021**, *17*, 1205–1209.

(22) Serrano, D.; Kuppusamy, S. K.; Heinrich, B.; Fuhr, O.; Hunger, D.; Ruben, M.; Goldner, P. Ultra-narrow optical linewidths in rare-earth molecular crystals. *Nature* **2022**, *603*, 241–246.

(23) Fataftah, M. S.; Bayliss, S. L.; Laorenza, D. W.; Wang, X.; Phelan, B. T.; Wilson, C. B.; Mintun, P. J.; Kovos, B. D.; Wasielewski, M. R.; Han, S.; Sherwin, M. S.; Awschalom, D. D.; Freedman, D. E. Trigonal Bipyramidal V3+ Complex as an Optically Addressable Molecular Qubit Candidate. *J. Am. Chem. Soc.* **2020**, *142*, 20400–20408.

(24) Wojnar, M. K.; Laorenza, D. W.; Schaller, R. D.; Freedman, D. E. Nickel(II) Metal Complexes as Optically Addressable Qubit Candidates. *J. Am. Chem. Soc.* **2020**, *142*, 14826–14830.

(25) Bayliss, S. L.; Laorenza, D. W.; Mintun, P. J.; Kovos, B. D.; Freedman, D. E.; Awschalom, D. D. Optically addressable molecular spins for quantum information processing. *Science* **2020**, *370*, 1309–1312.

(26) Laorenza, D. W.; Kairalapova, A.; Bayliss, S. L.; Goldzak, T.; Greene, S. M.; Weiss, L. R.; Deb, P.; Mintun, P. J.; Collins, K. A.; Awschalom, D. D.; Berkelbach, T. C.; Freedman, D. E. Tunable Cr4+ Molecular Color Centers. *J. Am. Chem. Soc.* **2021**, *143*, 21350–21363.

(27) Tanabe, Y.; Sugano, S. On the Absorption Spectra of Complex Ions. I. *J. Phys. Soc. Jpn* **1954**, *9*, 753–766.

(28) Roos, B. O.; Taylor, P. R.; Siegbahn, P. E. M. A Complete Active Space SCF Method (CASSCF) Using a Density Matrix Formulated Super-CI Approach. *Chem. Phys.* **1980**, *48*, 157–173.

(29) Siegbahn, P. E. M.; Almlöf, J.; Heiberg, A.; Roos, B. O. The Complete Active Space SCF (CASSCF) Method in a Newton–Raphson Formulation with Application to the HNO Molecule. *J. Chem. Phys.* **1981**, *74*, 2384–2396.

(30) Finley, J.; Åke Malmqvist, P.; Roos, B. O.; Serrano-Andrés, L. The multi-state CASPT2 method. *Chem. Phys. Lett.* **1998**, *288*, 299–306.

(31) Andersson, K.; Malmqvist, P. A.; Roos, B. O.; Sadlej, A. J.; Wolinski, K. Second-order perturbation theory with a CASSCF reference function. *J.Phys. Chem* **1990**, *94*, 5483–5488.

(32) Andersson, K.; Malmqvist, P.; Roos, B. O. Second-order perturbation theory with a complete active space self-consistent field reference function. *J. Chem. Phys.* **1992**, *96*, 1218–1226.

(33) Aquilante, F. et al. Molcas 8: New Capabilities for Multiconfigurational Quantum Chemical Calculations across the Periodic Table. *J. Comput. Chem.* **2016**, *37*, 506–541.

(34) Fdez. Galván, I. et al. OpenMolcas: From Source Code to Insight. *J. Chem. Theory Comput.* **2019**, *15*, 5925–5964.

(35) Li, Z.; Abramavicius, D.; Mukamel, S. Probing Electron Correlations in Molecules by Two-Dimensional Coherent Optical Spectroscopy. *J. Am. Chem. Soc.* **2008**, *130*, 3509–3515.

(36) Schapiro, I.; Sivalingam, K.; Neese, F. Assessment of n-Electron Valence State Perturbation Theory for Vertical Excitation Energies. *J. Chem. Theory Comput.* **2013**, *9*, 3567–3580.

(37) Pederson, M. R.; Jackson, K. A. Variational mesh for quantum-mechanical simulations. *Phys. Rev. B* **1990**, *41*, 7453–7461.

(38) Jackson, K.; Pederson, M. R. Accurate forces in a local-orbital approach to the local-density approximation. *Phys. Rev. B* **1990**, *42*, 3276–3281.

(39) Briley, A.; Pederson, M. R.; Jackson, K. A.; Patton, D. C.; Porezag, D. V. Vibrational frequencies and intensities of small molecules: All-electron, pseudopotential, and mixed-potential methodologies. *Phys. Rev. B* **1998**, *58*, 1786–1793.

(40) McCaskey, A.; Yamamoto, Y.; Warnock, M.; Burzurí, E.; van der Zant, H. S. J.; Park, K. Electron-vibron coupling effects on electron transport via a single-molecule magnet. *Phys. Rev. B* **2015**, *91*, 125419.

(41) Neese, F. Software update: the ORCA program system, version 4.0. *WIREs Comput. Mol. Sci.* **2018**, *8*, e1327.

(42) Bhandari, C.; Wysocki, A. L.; Economou, S. E.; Dev, P.; Park, K. Multiconfigurational study of the negatively charged nitrogen-vacancy center in diamond. *Phys. Rev. B* **2021**, *103*, 014115.

(43) Rubín-Osanz, M.; Lambert, F.; Shao, F.; Rivière, E.; Guillot, R.; Suaud, N.; Guihéry, N.; Zueco, D.; Barra, A.-L.; Mallah, T.; Luis, F. Chemical tuning of spin clock transitions in molecular monomers based on nuclear spin-free Ni(ii). *Chem. Sci.* **2021**, *12*, 5123–5133.

(44) Goldman, M. L.; Sipahigil, A.; Doherty, M. W.; Yao, N. Y.; Bennett, S. D.; Markham, M.; Twitchen, D. J.; Manson, N. B.; Kubanek, A.; Lukin, M. D. Phonon-Induced Population Dynamics and Intersystem Crossing in Nitrogen-Vacancy Centers. *Phys. Rev. Lett.* **2015**, *114*, 145502.

(45) Soykal, O. O.; Dev, P.; Economou, S. E. Silicon vacancy center in 4*H*-SiC: Electronic structure and spin-photon interfaces. *Phys. Rev. B* **2016**, *93*, 081207.

(46) Doherty, M. W.; Manson, N. B.; Delaney, P.; Jelezko, F.; Wrachtrup, J.; Hollenberg, L. C. The nitrogen-vacancy colour centre in diamond. *Phys. Rep.* **2013**, *528*, 1–45, The nitrogen-vacancy colour centre in diamond.

(47) Gali, A. Ab initio theory of the nitrogen-vacancy center in diamond. *Nanophotonics* **2019**, *8*, 1907 – 1943.

(48) Juban, E. A.; McCusker, J. K. Ultrafast Dynamics of 2E State Formation in Cr(acac)3. *J. Am. Chem. Soc.* **2005**, *127*, 6857–6865.

(49) Dorn, M. et al. A Vanadium(III) Complex with Blue and NIR-II Spin-Flip Luminescence in Solution. *J. Am. Chem. Soc.* **2020**, *142*, 7947–7955.

(50) Wegeberg, C.; Wenger, O. S. Luminescent First-Row Transition Metal Complexes. *JACS Au* **2021**, *1*, 1860–1876.

(51) Wolfowicz, G.; Heremans, F. J.; Anderson, C. P.; Kanai, S.; Seo, H.; Gali, A.; Galli, G.; Awschalom, D. D. Quantum guidelines for solid-state spin defects. *Nat. Rev. Mater.* **2021**, *6*, 906–925.

(52) Graham, M. J.; Yu, C.-J.; Krzyaniak, M. D.; Wasielewski, M. R.; Freedman, D. E. Synthetic Approach To Determine the Effect of Nuclear Spin Distance on Electronic Spin Decoherence. *J. Am. Chem. Soc.* **2017**, *139*, 3196–3201.

(53) Chen, J.; Hu, C.; Stanton, J. F.; Hill, S.; Cheng, H.-P.; Zhang, X.-G. Decoherence in Molecular Electron Spin Qubits: Insights from Quantum Many-Body Simulations. *J. Phys. Chem. Lett.* **2020**, *11*, 2074–2078.

(54) Perdew, J. P.; Wang, Y. Accurate and simple analytic representation of the electron-gas correlation energy. *Phys. Rev. B* **1992**, *45*, 13244–13249.

(55) Zope, R.; Baruah, T.; Jackson, K. A. FLOSIC 0.2, based on the NRLMOL code of M. R. Pederson.

(56) Pederson, M. R.; Ruzsinszky, A.; Perdew, J. P. Communication: Self-interaction correction with unitary invariance in density functional theory. *J. Chem. Phys.* **2014**, *140*, 121103.

(57) Bayliss, S. L.; Deb, P.; Laorenza, D. W.; Onizhuk, M.; Galli, G.; Freedman, D. E.; Awschalom, D. D. Enhancing Spin Coherence in Optically Addressable Molecular Qubits through Host-Matrix Control. 2022; `https://arxiv.org/abs/2204.00168`.

(58) Perdew, J. P.; Burke, K.; Wang, Y. Generalized gradient approximation for the exchange-correlation hole of a many-electron system. *Phys. Rev. B* **1996**, *54*, 16533–16539.

(59) Douglas, M.; Kroll, N. M. Quantum Electrodynamical Corrections to the Fine Structure of Helium. *Ann. Phys.* **1974**, *82*, 89–155.

(60) Hess, B. A. Relativistic Electronic-Structure Calculations Employing a Two-Component No-Pair Formalism with External-Field Projection Operators. *Phys. Rev. A* **1986**, *33*, 3742–3748.

(61) Dunning, T. H. Gaussian basis sets for use in correlated molecular calculations. I. The atoms boron through neon and hydrogen. *J. Chem. Phys.* **1989**, *90*, 1007–1023.

(62) de Jong, W. A.; Harrison, R. J.; Dixon, D. A. Parallel Douglas-Kroll energy and gradients in NWChem: Estimating scalar relativistic effects using Douglas-Kroll contracted basis sets. *J. Chem. Phys.* **2001**, *114*, 48–53.

(63) Hess, B. A.; Marian, C. M.; Wahlgren, U.; Gropen, O. A Mean-Field Spin-Orbit Method Applicable to Correlated Wavefunctions. *Chem. Phys. Lett.* **1996**, *251*, 365 – 371.

(64) Malmqvist, P.-Å.; Roos, B. O.; Schimmelpfennig, B. The Restricted Active Space (RAS) State Interaction Approach with Spin-Orbit Coupling. *Chem. Phys. Lett.* **2002**, *357*, 230–240.

(65) Ghigo, G.; Roos, B. O.; Åke Malmqvist, P. A modified definition of the zeroth-order Hamiltonian in multiconfigurational perturbation theory (CASPT2). *Chem. Phys. Lett.* **2004**, *396*, 142–149.

(66) Roos, B. O.; Andersson, K. Multiconfigurational perturbation theory with level shift — the Cr2 potential revisited. *Chem. Phys. Lett.* **1995**, *245*, 215–223.

(67) Chibotaru, L. F.; Ungur, L. Ab Initio Calculation of Anisotropic Magnetic Properties of Complexes. I. Unique Definition of Pseudospin Hamiltonians and their Derivation. *J. Chem. Phys.* **2012**, *137*, 064112.

(68) Wysocki, A. L.; Park, K. Nature of Hyperfine Interactions in TbPc2 Single-Molecule Magnets: Multiconfigurational Ab Initio Study. *Inorg. Chem.* **2020**, *59*, 2771–2780.